HIGH RESOLUTION WALL-SHEAR STRESS MEASUREMENTS USING A MICRO-PILLAR SENSOR MPS^3

Sebastian Große and Wolfgang Schröder
Institute of Aerodynamics,
RWTH Aachen University
Wüllnerstraße 5-7, D-52062 Aachen, Germany
s.grosse@aia.rwth-aachen.de

ABSTRACT

Measurements of the mean and fluctuating wall-shear stress in fully developed turbulent pipe flow at Reynolds number Re_b based on the bulk velocity and the pipe diameter D ranging from $Re_b = 5000 - 20000$ were performed using the micro-pillar shear-stress sensor MPS^3. The Reynolds number based on the skin-friction velocity ranges from $Re_\tau = 340$ to 1150. The results demonstrate a convincing agreement of the mean wall-shear stress obtained with the new sensor technique with analytical and experimental results from the literature. A first estimate of the pillar dynamic response will be derived and first results from measurements of the fluctuating wall-shear stress in turbulent pipe flow will be discussed and compared to results from the literature.

INTRODUCTION

The assessment of the wall-shear stress $\tau = \eta \cdot \partial u/\partial y|_{wall}$ has been the subject of many experimental and numerical studies in the last decades. Herein, η is the dynamic fluid viscosity, u the streamwise velocity and y the distance from the wall. The knowledge of the mean wall-shear stress is a necessary prerequisite to determine the friction velocity $u_\tau = (\tau/\rho)^{1/2}$ as one of the fundamental turbulence scaling parameters. Herein, ρ is the fluid density. The temporal and spatial shear-stress distribution is related to turbulent flow structures in the vicinity of the wall and as such is of major importance for the basic understanding of the development of near-wall turbulent events.

Recently developed wall-shear stress sensors can be divided into two major categories based on the measurement principle, the so-called direct and indirect techniques. Wall-implemented floating elements and oil-film techniques are the most common representatives of the former technique. Indirect techniques require an empirical or theoretical relation between the wall-shear stress and the quantity measured by the sensor. Typically this relation is only valid for very specific conditions. Comprehensive reviews on the development of wall-shear stress devices are given by Löfdahl and Gad-el-Hak (1999), and Naughton and Sheplak (2002).

Most existing sensors are one-directional devices that require the necessity of secondary electronic structures to be implemented in the wall, thereby impeding the spatial resolution and limiting the arrays to a maximum number of sensors due to constructional constraints. The micro-pillar shear-stress sensor *MPS*^{3} minimizes these problems and enables an easy assessment of the spatial wall-shear stress distribution.

DESCRIPTION OF THE MICRO-PILLAR SENSOR MPS^3

The sensor principle is based on thin cylindrical structures, which bend due to the fluid forces. The wall-shear stress is derived indirectly from its relation to the detected velocity gradient in the viscous sublayer. The pillars are manufactured from the elastomer polydimethylsiloxane (PDMS) at diameters D_p in the range of microns. A single pillar is shown in figure 1(a).

The flexibility of the material ensures a high sensitivity of the sensor. The low intrusiveness of the sensor due to the symmetric and smooth curvature has been examined using μPIV of the local flow field around the pillar structure in Große et al. (2006). The results showed the flow past the pillar to be well in the Stokes-flow regime for most turbulent flows of interest.

The sensor concept allows the two-dimensional detection of fluid forces, since the symmetric geometry has no preferred sensitivity direction. Thus, the micro-pillar sensor technology enables to measure the two wall-parallel components of the drag force. The optical detection principle leads to an extremely high local resolution of the planar wall-shear distribution. The impeding limitation is the local disturbance of the flow field by the pillar structure and the interference of neighboring pillars. However, due to the Stokes flow, there is only a local impact on the flow field in a region of two to four diameters downstream of the sensor (Große et al., 2006) such that an extremely high spatial resolution can be achieved. There exist no additional constraints due to the placement of necessary secondary structure or data read-out devices. The sensor structure has a minimum dimension in the wall-parallel plane thereby reducing the spatial averaging. For typical Reynolds numbers the dimension of the sensor in viscous units is $L_p^+ \leq 1$, where $L_p^+ = u_\tau D_p/\nu$, where $\nu = \eta/\rho$.

To enable a sufficiently high sensitivity the sensor possesses an optimum height under the restriction of the validity of the linear relation between the wall-shear stress and the near-wall velocity gradient. That is, the sensor needs to be fully immersed in the flow field for which the linear velocity gradient is guaranteed. For most turbulent flows of low to moderate Reynolds numbers the height of the viscous sublayer is in the order of 80 to 1000 μm.

MECHANICAL MODELS FOR THE MPS^3 SENSOR

Mechanical Model for Static Micro-Pillar Response

A mechanical model for the sensor often used is that of a clamped cylindrical beam under linear shear load (figure 1(b)). In the following, it will be shown that the simplifying assumptions are too rigorous to describe the sensor behavior in linear shear flow making an experimental static sensor calibration a necessary prerequisite.

The cylindrical sensor protrudes from the wall into the very near-wall flow region and bends due to the fluid forces exerted on the structure. Consequently, the sensor deflection, and hence, the sensor-tip deflection, serve as a measure for the wall-shear stress. For wall distances $y^+ \leq 5$, i.e., within the viscous sublayer, the velocity gradient is approximated by $\partial u/\partial y = U(y)/y$, and hence, the wall-shear stress $\tau = \eta \cdot \partial u/\partial y|_{wall}$ becomes $\tau = \eta \cdot U(y)/y$.

To estimate the pillar bending, the mean forces exerted on the cylindrical structure in plain shear flow can be calculated using the Oseen-approximation for the drag load per unit length of the cylinder (Bairstow et al., 1923)

$$q(y) \approx \frac{4\pi\eta}{2 - log_e(Re_{D_p}(y))} \cdot U(y). \qquad (1)$$

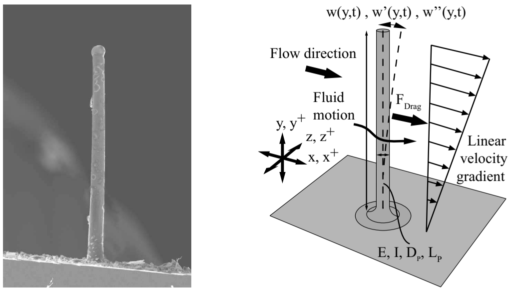

Figure 1: Scanning electron microscope images (left) of a single pillar and (right) mechanical model of the pillar sensor.

Herein, $\gamma = 0.577$ is the Euler constant. Some authors derive a value of $q(y) = 4\pi\eta / ln(L_p/(2D_p)) \cdot U(y)$ for the drag force from the Oseen approximation with L_p being the sensor length. However, there is no clear reasoning to further linearize equation 1 leading to this simplified force term. Furthermore, the derivation of the Oseen drag assumes an infinite cylinder length and as such the influence of the cylinder length L_p on the drag force is rather questionable.

The assumption of Oseen flow around the sensor structure is valid as long as the Reynolds number $Re_{D_p} = U_{L_p} D_p / \nu$ defined by the pillar diameter D_p and the maximum velocity U_{L_p} at the pillar tip, i.e. at $y = L_p$, is $Re_{D_p} \ll 1$, which is generally the case.

Assuming the sensor being represented by a one-sided clamped cylinder bent by the viscous forces and a linear gradient of the mean velocity in the viscous sublayer, the deflection $w(L_p)$ of the pillar tip can be determined numerically

$$w''''(y) = (EI)^{-1} \cdot q(y) \, , \tag{2}$$

by satisfying the boundary conditions $w'''(L_p) = w''(L_p) = w'(0) = w(0) = 0$. Figure 2(a) shows the theoretical deflection of the pillar tip $w(L_p)$ as a function of the maximum local Reynolds number $Re_{D_p}(L_p)$ at the pillar tip. Note, $Re_{D_p}(L_p)$ was kept ≤ 1 to ensure the validity of Oseen's approximation for the drag force. The deflection in figure 2(a) evidences a slightly non-linear reaction of the theoretical pillar deflection to a linear increase in the Reynolds number Re_{D_p}, i.e., to a linear increase of the velocity field along the sensor structure. This non-linearity exists over the whole range of $0 \leq Re_{D_p}(L_p) \leq 1$.

However, experimental results clearly showed a linear bending of the pillar structure up to even high deflections $w(L_p)/L_p$ during rheometer calibration. That is, those measurements did not corroborate the findings from the analytical estimate. Consequently, the assumption of the pillar behaving like a clamped cylinder bent by the fluid forces and following linear bending theory seems to be too rigorous. It is rather obvious that additional effects such as the stiffening of the material due to the deflection from its straight position and a lowering of the pillar tip as a consequence of the bending have to be taken into account to obtain an appropriate mechanical model of the pillar bending.

Thus, an experimental calibration of the pillar deflection is required to determine the relation between the mean wall-shear stress and the pillar bending.

Static Calibration of the Sensor

The static calibration process is described in more detail in Große et al. (2006). Here, only a brief overview is given. A calibration of the micro-pillars can be performed in a plate-cone rheometer, since such devices generate a plane linear shear flow with constant shear rate over a sufficiently wide spatial region and velocity range such that the drag force distribution exerted on the sensor structure is identical to that in the viscous sublayer of a turbulent boundary layer.

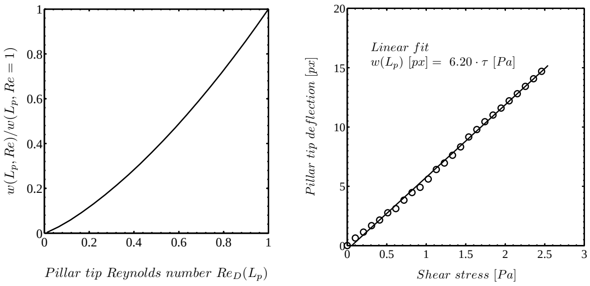

Figure 2: (left) Deflection of pillar tip as a function of the maximum Reynolds number Re_{D_p}. Exemplary pillar-tip deflection (right) during pillar calibration in plate-cone rheometer flow.

Probability density functions of fluctuating wall-shear stress in turbulent flow evidence the maximum possible values to be about three times as high as the mean wall-shear stress and hence, it is necessary to perform a static calibration of the sensor up to such high values. Since maximum mean wall-shear stress values in the order of 0.85 *Pa* are expected in the investigated pipe flow the static sensor calibration was performed up to 2.5 *Pa*.

The results of the static calibration in figure 2(b) demonstrate a linear behavior between applied shear stress and pillar bending up to extremely high rotation rates of the rheometer calibration device.

Mechanical Model for the Dynamic Micro-Pillar Response

To accurately capture the complete frequency spectrum with the MPS^3 sensor, it is necessary to know the frequency response function $G(f)$ of the sensor structure, where f is the excitation frequency. Since the static estimate has shown only some minor discrepancy between the theoretical approximation and the results from the static calibration, the structure will in a first attempt be assumed as a one-side clamped cantilever. The diameter of the pillar varies only slightly along the pillar axis and can be assumed constant such that the cross section $A(y) = A$, the second moment of inertia $I(y) = I$, and the mass distribution $\rho \cdot A$ are uniformly distributed along the sensor length. Consequently, the one-dimensional linear Euler-Bernoulli governing equation of motion of the micro-pillar sensor can be expressed as

$$\chi \cdot E \cdot I \cdot \frac{\partial^4}{\partial y^4} \left(\frac{\partial w(y,t)}{\partial t} \right) + E \cdot I \cdot \frac{\partial^4 w(y,t)}{\partial y^4} + \rho A \cdot \frac{\partial^2 w(y,t)}{\partial t^2} = F(y,t) \, . \tag{3}$$

Herein, χ is the damping coefficient per unit length due to internal viscous damping of the sensor material. $w(y,t)$ is the lateral displacement of the pillar sensor at a distinct height y and time t. The term $F(y,t)$ on the right hand side of equation 3 represents the external force per unit length and will be discussed in detail in the following.

With the assumption of the sensor structure being immersed in the viscous sublayer, the flow field can be assumed to possess a linear velocity gradient in the wall-normal direction and hence, to vary only slowly along the pillar length leading to a two-dimensional flow field in a wall-parallel plane. The local flow field and hence the forces exerted on the sensor structure over an incremental length of the pillar are consequently the same as the flow field around an infinitely long rigid beam executing transverse oscillations with the same amplitude.

To achieve the frequency response function of the sensor structure on an oscillating fluid excitation, the velocity field will be assumed to perform a sinusoidal movement perpendicular to the primary axis of the sensor at a constant frequency. Note, the fluid forces exerted on the pillar structure depend on the relative velocity between sensor and fluid, which can be expressed as

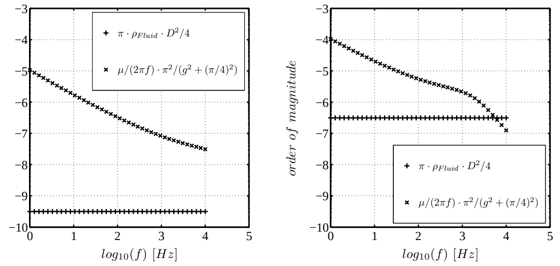

Figure 3: Comparison of the second and third term in the mass coefficient of the pillar equation of motion for water (left) and air (right) as functions of the excitation frequency f.

$$u_{rel.}(y,t) = U_{L_p} \cdot y/L_p \cdot ((\sin 2\pi f t + \xi_S) - \dot{w}(y,t)) \; . \qquad (4)$$

Herein, U_{L_p} is the local peak velocity at the edge of the viscous sublayer, $\dot{w}(y,t)$ is the sensor velocity, and ξ_S an arbitrary phase shift.

The resulting forces will be assumed using Stokes' solution for an infinite cylinder moving in viscous fluid with a sinusoidal velocity (Stokes, 1922). The force $F(y,t)$ per unit length exerted on the cylinder is given by

$$\begin{aligned} F(y,t) = & \left\{ 4\pi\mu \cdot \frac{-g}{g^2+(\pi/4)^2} \right\} \cdot u_{rel.}(y,t) \\ & + \left\{ \pi\rho_{fluid}\frac{{D_p}^2}{4} + \frac{\mu}{2\pi f} \cdot \frac{\pi^2}{g^2+(\pi/4)^2} \right\} \cdot \dot{u}_{rel.}(y,t) \; , \qquad (5) \end{aligned}$$

where $g = ln(s) + \gamma$, $s = D_p/4 \cdot \sqrt{(2\pi f/\nu)}$, and $\gamma = 0.577$ is the Euler constant. Note, the first term in equation 5 describes a drag force resulting from dissipative effects due to the fluid viscosity, whereas the second term can be interpreted as an additional mass added to the pillar structure, which is proportional to the pillar acceleration.

To couple fluid and structural mechanics it is only necessary to insert equation 5 into equation 3 for the pillar motion leading to

$$\begin{aligned} & \chi \cdot E \cdot I \cdot \frac{\partial^4}{\partial y^4}\left(\frac{\partial w(y,t)}{\partial t}\right) + E \cdot I \cdot \frac{\partial^4 w(y,t)}{\partial y^4} + \\ & \left\{ \pi\rho_{PDMS}\frac{{D_p}^2}{4} + \pi\rho_{Fluid}\frac{{D_p}^2}{4} + \frac{\mu}{2\pi f} \cdot \frac{\pi^2}{g^2+(\pi/4)^2} \right\} \cdot \frac{\partial^2 w(y,t)}{\partial t^2} + \\ & \left\{ 4\pi\mu \cdot \frac{-g}{g^2+(\pi/4)^2} \right\} \cdot \frac{\partial w(y,t)}{\partial t} = \\ & \left\{ \pi\rho_{Fluid}\frac{{D_p}^2}{4} + \frac{\mu}{2\pi f} \cdot \frac{\pi^2}{g^2+(\pi/4)^2} \right\} \cdot U_L \cdot y/L \cdot (\sin(2\pi f t + \xi_S)) + \\ & \left\{ 4\pi\mu \cdot \frac{-g}{g^2+(\pi/4)^2} \right\} \cdot U_L \cdot y/L \cdot 2\pi f \cdot \cos(2\pi f t + \xi_S) \; . \qquad (6) \end{aligned}$$

This is a fourth-order differential equation for $w(y,t)$, which can be solved numerically using the boundary conditions $w|_{y=0} = \partial w/\partial y|_{y=0} = 0$ and $\partial^2 w/\partial y^2|_{y=L} = \partial^3 w/\partial y^3|_{y=L} = 0$.

Further simplifications are possible when regarding the terms in equation 6. The first term in the mass term is due to the mass of the pillar material, the second due to the mass of the displaced fluid. It is obvious that the ratio of these two terms depends only on the different densities of structure and fluid and hence, the second term can be neglected when the pillar is used in air. On the other hand, when the pillar is used in water, the fluid density is in the same order of magnitude as the sensor density and has to be accounted for. The third term depends on the excitation frequency and needs a further investigation. In figure 3 the second and third term of the mass term are juxtaposed and demonstrate that in water and air the third term is at least one order of magnitude larger than the second term in the relevant frequency range.

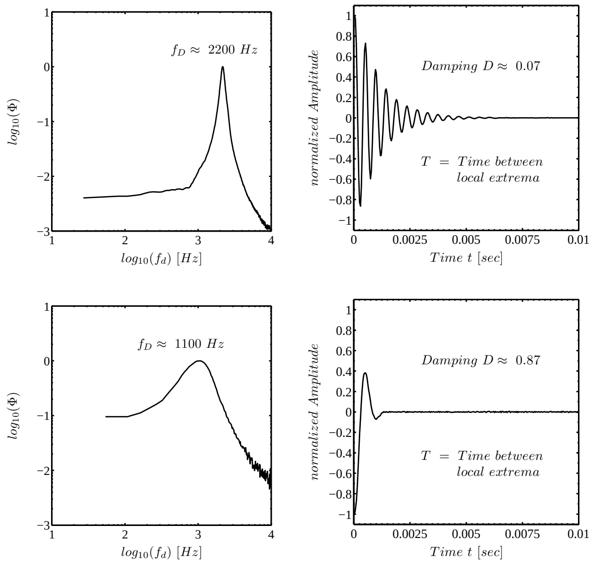

Figure 4: Power spectral density Φ (left) of the pillar deflection in air (upper) and water (lower). Time response (right) of the pillar to an excitation.

Approximate Pillar Dynamics

The detailed numerical solution of equation 6 will not be given in this paper. A reduced order approximation of the pillar dynamics will be given based on characteristic dynamic parameters, which have been obtained experimentally.

It can be shown that the fourth-order partial differential equation can be reduced to an ordinary second-order differential equation

$$\frac{\partial^2 w(y,t)}{\partial t^2} + 2D \cdot (2\pi f_0)\frac{\partial w(y,t)}{\partial t} + (2\pi f_0)^2 \cdot w(y,t) = 0 \; , \qquad (7)$$

the solution of which is well known. Herein, D is the damping coefficient and f_0 the undamped eigen-frequency. The damping coefficient D in equation 7 and the damped eigen-frequency f_D can by found experimentally by determining the pillar step response. The results in figure 4 show the damping coefficient to be $D \approx 0.07$ in air and $D \approx 0.87$ in water. The corresponding damped eigen-frequencies are $f_D \approx 2200$ and $f_D \approx 1100$, respectively. Applying $f_0 = f_D \cdot \sqrt{(1-D^2)}$ gives an $f_0 \approx 2100 - 2200$. The transfer function for a system described by equation 7 with a damping coefficient $0.7 \leq D \leq 1$ can in a first step be assumed approximately constant for frequencies lower than $0.3 - 0.4 \; f_0$.

Since the maximum expected turbulent frequencies for the investigated Reynolds number range is approximately 800 Hz they occur in the regime of a constant sensor transfer function.

EXPERIMENTAL SETUP

Flow Facility

The experiments were performed in a pipe facility at the Institute of Aerodynamics. The pipe possesses a diameter of $D = 40 \; mm$. The fluid used in the measurements is deionised water at $T = 20°C$. During the measurements the temperature varies less than $0.1°C$. The

Reynolds number based on the bulk velocity $Re_b = U_b D/\nu$ is determined from the measured volume flux V.

The flow enters through a flow straightener with 5 mm core size followed by a 0.2 mm fine mesh. The straightener enters into the pipe measurement section with a tripping device installed 40 D upstream of the measurement position. The tripping device consists of a circular ring generating a contraction ratio of 0.85. The fluid exits the measurement section into an open reservoir and flows through a heat exchanger to maintain a constant fluid temperature.

Particle-image velocimetry (PIV) measurements at Reynolds numbers Re_b ranging from $5000 - 20000$ confirm the character of the fully developed turbulent pipe flow in the measurement section to be consistent with experimental and numerical results from the literature.

For turbulent pipe flow values of the wall-shear stress are well known, such that a comparison of the experimental results with the data from the literature will allow to evaluate the capability of the sensor MPS^3 to determine the mean turbulent wall-shear stress. Generally, the wall-shear stress can be expressed by

$$\tau = \lambda \rho {U_b}^2/8 \,, \tag{8}$$

where λ is the friction factor. For turbulent flow in a smooth circular pipe, Prandtl and von Karman (Schlichting (1958)) provide a formula for the friction factor λ

$$\frac{1}{\sqrt{\lambda}} = 2.0 \cdot log_{10}\left(Re_b\sqrt{\lambda}\right) - 0.8 \,. \tag{9}$$

This allows to easily determine the theoretical wall-shear stress for turbulent pipe flow and also the Reynolds number based on the friction velocity Re_τ.

Micro-Pillar Sensor Setup

The micro-pillar sensor that is used for measurements of the wall-shear stress is mounted in a 1 *mm* cannula, which can be placed very exactly through a hole in the pipe wall. Note, the maximum local disturbance due to the flat surface of the sensor mount is $\approx 3 \cdot 10^{-4}$ D, which corresponds to 0.17 y^+ at the highest Reynolds numbers in the experiments, i.e., additional disturbances can be neglected. The micro-pillar has a height L_p of 370 μm and a mean diameter D_p of approximately 20 μm. The height corresponds to about 3-7 viscous units for most Reynolds numbers in the experiments. Only at the highest Reynolds numbers the sensor exceeds the viscous sublayer with a height of $y^+ = 10$. However, the results in the following section evidence the sensor to still correctly detect the value of the mean wall-shear stress in pipe flow even under these conditions.

Optical Detection and Accuracy

The sensor displacement from a reference position at no velocity is observed using a highly magnifying macro lens mounted on a Fastcam 1024 PCI high-speed camera. The setup in the experiments matches that for the pillar calibration in the rheometer. The camera is operated at 125 Hz and 2000 Hz. 51200 images are recorded for each measurement at both recording frequencies resulting in a total period of 7 *min* and 25 *sec* respectively. During this timespan a particle with bulk velocity U_b travels a distance of $2600 - 5200$ D at 125 *Hz* and $160 - 320$ D at 2000 *Hz* depending on the Reynolds number.

With the magnification of the optical system the mean deflection of the pillar tip ranges between $2 - 12$ *px* depending on the Reynolds number. The pillar tip can be detected as a bright single spot with a diameter of $2 - 4$ *px* on the recorded images. Two additional reference spots on the sensor mount are used to correct a possible vibration of the camera. Since the pillar tip represents a single spot the data is correlated via a Gaussian template.

The evaluation is performed using PIV-correlation routines with multi-passing. To test the accuracy under experimental conditions the pillar position at zero flow with an artificially induced vibration was evaluated. The vibration can be detected via identifying the movement of the reference spots. With this procedure, the inaccuracy in determining the pillar tip and the sensor mount is included. The resulting rms value of the pillar deflection was 0.07 *px* and the error to determine the pillar-tip displacement becomes less than 2.5%.

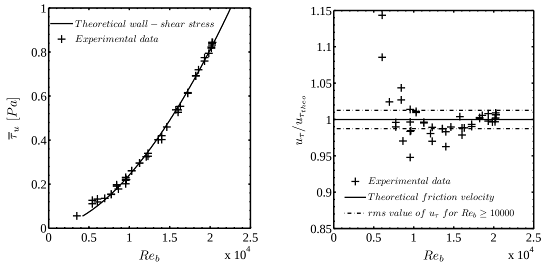

Figure 5: Mean streamwise wall-shear stress $\overline{\tau}_u$ (left) compared to the solution calculated with formula 8 and 9. Ratio of the friction velocity u_τ (right) obtained experimentally with the proposed method and the theoretical friction velocity $u_{\tau_{theo}}$.

RESULTS

Measurements of the mean wall-shear stress have been performed for turbulent pipe flow at a variety of Reynolds numbers Re_b ranging from $5000 - 20000$. Data for the evaluation of the fluctuating wall-shear stress have been recorded at four different Reynolds numbers $Re_b = 10000, 15000, 17750,$ and 20000. First, the results for the mean wall-shear stress will be discussed. In the following, a first outlook on the determination of the fluctuating wall-shear stress will be given. With the estimate for the pillar response, the pillar transfer function was assumed to be constant in the complete frequency range.

Mean Wall-Shear Stress

In figure 5 the results from the present experimental study are juxtaposed to values calculated by equations 8 and 9 for the friction factor for turbulent flow in hydraulically smooth pipes. The results show excellent agreement with the analytical estimates and evidence the sensor to be capable of correctly detecting the mean wall-shear stress in turbulent flows.

At the lowest Reynolds numbers in the experiments, i.e., for $Re_b \leq 10000$, the data scatter around the theoretical value of the mean wall-shear stress. This can also be observed in figure 5(b), where the measured friction velocity u_τ is compared with theoretical values calculated by equation 9. The higher error in the estimate of the wall-shear stress is due to the very low values of the mean wall-shear stress of ≈ 0.1 *Pa* and the chosen optical resolution during the measurements leading to a pillar-tip deflection in the order of $1 - 2$ *px* and hence, to an increased error in the estimate of the wall-shear stress.

The use of higher magnifying optics especially at low Reynolds numbers would increase the optical resolution and hence, would allow a higher accuracy of the system. Furthermore, the use of more slender pillars with higher deflections would enhance the sensitivity of the wall-shear stress sensor principle.

The results at $Re_b \geq 10000$ scatter only slightly around the theoretical value of the mean wall-shear stress $u_{\tau_{theo}}$ and allow to determine the mean wall-shear stress with an rms value of $\approx 1.25\%$ of $u_{\tau_{theo}}$ under the current experimental conditions. The rms value calculated from the results at $Re_b \geq 10000$ is also plotted in figure 5(b).

Although the sensor with a height of $L_p = 370$ μm partly exceeds the viscous sublayer for $Re_b \geq 13000$, the detected wall-shear stress follows the predicted trend.

Wall-Shear Stress Intensity, Skewness and Flatness

While the linear behavior of the mean velocity gradient in the viscous sublayer is commonly accepted, there are controversial results and opinions on the fluctuation intensity $u'/\overline{U}$ in the literature, where $\overline{U}$ is the mean streamwise velocity. Often a value of $u'/\overline{U}\big|_{wall} \equiv \tau_u{}'/\overline{\tau}_u = 0.4$ at the wall is assumed, where $\overline{\tau}_u$ is the mean wall-shear stress. Note, the wall-shear stress and velocity fluctuations, $\tau_u{}'/\overline{\tau}_u$ and $u'/\overline{U}$, respectively, are directly related to each other in the vicinity of the wall and as such can be directly compared.

The distribution of the fluctuations in the viscous sublayer is of major importance for indirect measurement techniques. For channel flow, Kreplin and Eckelmann (1979) report a value of $u'/\overline{U} = 0.25$ at the wall with a plateau at $y^+ = 3-6$ and values of $u'/\overline{U} = 0.36$ to 0.37 before the fluctuation intensity decays. Wietrzak and Lueptow (1994) compile several results from experimental studies and DNS results for channel and boundary layer flow with values of $\tau_u{}'/\overline{\tau}_u$ ranging from 0.1 to 0.4. Alfredsson et al. (1988) found the values of $u'/\overline{U}$ to be at a constant level of 0.4 up to values of $y^+ = 4$ in turbulent channel flow, a trend that is also supported by the results obtained by Khoo et al. (1997). For higher values of y^+, the authors report the rms value to decrease to $0.33-0.3$. Numerical calculations for channel flow performed by Moser et al. (1999) for Reynolds numbers ranging from $Re_b = 5600$ to 21000 showed the values to be $\tau_u{}'/\overline{\tau}_u = 0.38-0.4$.

Figure 6(a) shows the measured rms values $\tau_u{}'/\overline{\tau}_u$ to be approximately 0.39 for the streamwise component at the lowest Reynolds number in the experiments and to decrease with the Reynolds number to values of $\tau_u{}'/\overline{\tau}_u = 0.33-0.34$ in the range of $Re_b = 10000$ to 20000. The micro-pillar sensor protrudes further into the near-wall region at higher Reynolds numbers and this causes a spatial averaging up to higher values of y^+, i.e., the observed decrease in the present study is in good agreement with the findings of Khoo et al. (1997) and Alfredsson et al. (1988). Consequently, it has to be taken into account that the sensor integrates the flow field along the wall-normal direction and hence, a gradient of any flow property along the sensor length can hardly be detected. Therefore, at the present state, it cannot be determined from the results obtained with the actual setup whether or not the intensity of the wall-shear stress fluctuations $\tau_u{}'/\overline{\tau}_u$ is constant within the viscous sublayer. It can only be stated that the mean value of $\tau_u{}'/\overline{\tau}_u$ in the vicinity of the wall is represented by the values noted above.

The measured spanwise component $\tau_w{}'/\overline{\tau}_u$ in figure 6(a) is about 0.15 at the lowest Reynolds number in the experiments. At higher Reynolds numbers the intensity decreases to values of $\tau_w{}'/\overline{\tau}_u \approx 0.13$. This is in good agreement with the findings of Kreplin and Eckelmann (1979). Their results show the spanwise component to reach a maximum intensity of $\tau_w{}'/\overline{\tau}_u = 0.2$ at wall distances $y^+ = 3-4$ followed by a strong decay to values of approximately 0.1. Note, the pillar sensor tends to average the slope of the fluctuation intensity $\tau_w{}'/\overline{\tau}_u$ and to underestimate the value in the vicinity of the wall. Using smaller pillars with $L_p = 3-4\,y^+$ would reduce this effect.

The skewness of the fluctuations in figure 6(b) is $S_f(\tau) = 0.85$ at the lower Reynolds numbers and decreases slightly to $S_f(\tau) = 0.6$ at higher Reynolds numbers. Values of $S_f(u) \approx 1.0$ are reported in Alfredsson et al. (1988) and in Khoo et al. (1997) for hot-wires located at $y^+ \leq 4$ whereas Fernholz and Finley (1996) report a $S_f(u)$ of $1.2 \div 1.3$ in the near-wall region and a vanishing $S_f(u)$ at values of $y^+ \geq 12$.

The findings for the flatness $F_f(\tau)$ in figure 6(b) show a similar behavior. It reaches $F_f(\tau) = 3.7$ at lower Reynolds numbers and decreases to a value of 3.1 at higher Reynolds numbers. Similarly high values are reported in Fernholz and Finley (1996) at $y^+ \leq 4$.

Note, the flatness and skewness of the velocity fluctuations are reported to decay strongly with increasing y^+. The decreasing skewness and flatness at higher Reynolds numbers result from an inadequate sensor length and an integration of fluctuations along the wall-normal direction up to higher values of y^+.

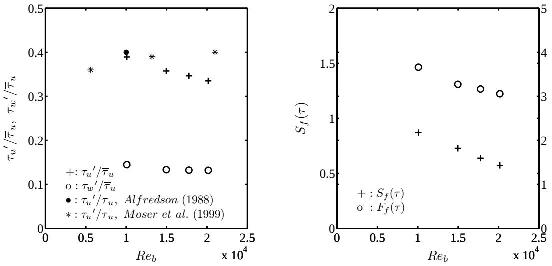

Figure 6: RMS values (left) of the streamwise $\tau_u{}'/\overline{\tau}_u$ and spanwise wall-shear stress fluctuations $\tau_w{}'/\overline{\tau}_u$. Skewness $S_f(\tau)$ and flatness $F_f(\tau)$ (right) of the streamwise wall-shear stress fluctuations τ_u'.

Frequency Spectra

The frequency spectra of the streamwise wall-shear stress fluctuations τ_u are plotted in figure 7. Spectral densities $\Phi^+(f^+)$ have been calculated using the formula given in Press et al. (1992). For each recording frequency the power spectra have been normalized such that $\int_0^\infty \Phi^+(f^+) df^+ = \tau_u{}'$. The spectral densities $\Phi^+(f^+)$ and frequencies f^+ are scaled with inner and outer variables as well as with a combination of both, i.e., a mixed scaling is applied.

It can be concluded from the results that mixed scaling provides the best collapse of the complete frequency spectra. The high-frequency parts of the fluctuations collapse best for inner and mixed scaling, whereas outer scaling leads to diverging spectral densities at the high frequencies. The low-frequency parts of the fluctuations collapse best for mixed scaling, whereas inner scaling causes a strong spread of the spectral densities distributions at low frequencies. This result is also reported by Alfredsson and Johansson (1984) and Jeon et al. (1999) for spectral densities obtained experimentally and from DNS of turbulent channel flow.

The question whether or not wall-shear stress or velocity fluctuations in the near-wall region of turbulent boundary layers, i.e., the buffer layer or low logarithmic region scale with inner or outer variables has very controversially been discussed.

Most authors applied inner scaling to their results from the buffer region but it seems that mixed scaling would have rather led to the Reynolds number independence of the data. Madavan et al. (1985) shows results from skin-friction measurements in turbulent boundary layer flow at different Reynolds numbers and assumes wall-shear stress spectra to scale with inner variables. The spectral data presented contains only the low frequency end of the complete frequency spectrum such that it is hard to know whether or not the applied scaling also holds for the high frequency content of the turbulent fluctuations. Alfredsson and Johansson (1984) report velocity fluctuations in the buffer layer of turbulent channel flow at Reynolds numbers Re_b between 13800 and 123000 to collapse best when mixed scaling is applied. The experimental results from Sreenivasan and Antonia (1977) and Madavan et al. (1985) were juxtaposed by Jeon et al. (1999) and evidence no reasonable collapse of the spectral densities in a Reynolds number range $Re_\tau = 289-3060$ when inner or outer scaling is applied. As mentioned before this contradicts with the inner scaling that Madavan et al. (1985) applied to their own data.

It can be suggested from the present results, that the use of mixed scaling variables, which seems most reasonable as scaling parameters for velocity fluctuations in the buffer region and further away in wall-bounded flows, also applies for the wall-shear stress fluctuations over the investigated Reynolds number range for turbulent pipe flow.

Nonetheless, it has to be kept in mind that the scaling of power spectra is very sensitive to the determination of the correct friction velocity. Furthermore, the experimental determination suffers strongly from spatial averaging caused by an inappropriate dimension of the detection devices, i.e., especially small scale structures are affected

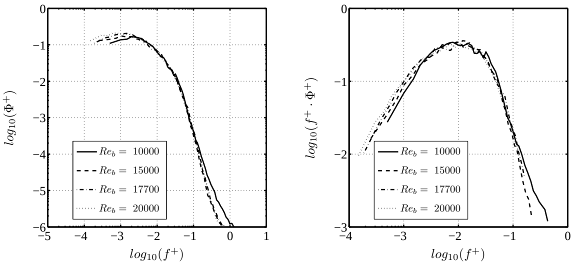

(a) inner scaling (b) inner scaling

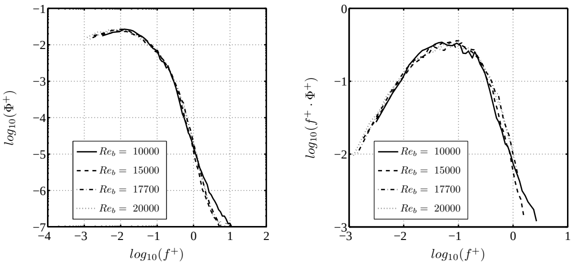

(c) mixed scaling (d) mixed scaling

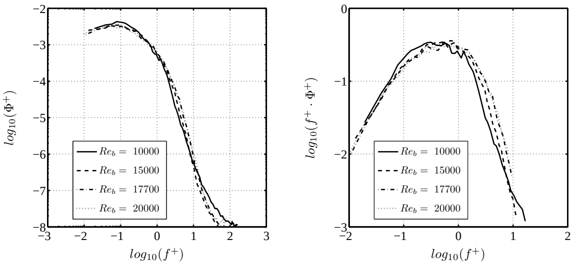

(e) outer scaling (f) outer scaling

Figure 7: Power spectra Φ^+ (left) and pre-multiplied power spectra $f^+\Phi^+$ (right) of τ_u as functions of the frequency f^+ in inner, mixed, and outer scaling at different Reynolds numbers.

by the integration of the turbulent signal along the sensor dimensions.

Pre-multiplied power spectra showing $f^+\Phi^+$ versus f^+ are also given in figure 7. This allows to easily recognize the frequency range of the energy containing vortices. The results show a maximum in the spectral power $f^+\Phi^+$ for inner scaling at $f\nu/u_\tau^2 \approx 10^{-2}$ and for outer scaling at $f\delta/U_0 \approx 4-5\cdot 10^{-1}$.

CONCLUSION

A new sensor concept based on flexible micro-pillars to measure the two-dimensional wall-shear stress distribution in turbulent flow has been introduced. Results of the mean wall-shear stress in turbulent pipe flow at Re_b ranging from $5000-20000$ are in convincing agreement with data available from the literature. They evidence the micro-pillar shear-stress sensor MPS^3 to correctly detect the mean wall-shear stress with an error of $\approx 1.25\%$ at the higher Reynolds numbers in the experiments.

A rough estimate of the sensor based on experimental data has been presented showing the sensor to have a constant dynamic transfer function up to ≈ 800 *Hz*, such that the evaluation of the fluctuating wall-shear stress in turbulent pipe flow at the investigated Reynolds numbers could be performed. The preliminary results have demonstrated convincing agreement with data from the literature.

The sensor needs no additional infrastructure on the wall and possesses the advantage of very low flow interference. The sensor concept is reasonably robust and can easily be mounted on almost any surface. Pillars can be manufactured in a large diversity of aspect ratios and heights enabling a perfect adaptation of the sensor to the flow.

REFERENCES

Alfredsson, P. H., Johansson, A. V., Haritonidis, J. H., and Eckelmann, H. 1988. “The fluctuating wall-shear stress and the velocity field in the viscous sublayer”. *Physics of Fluids*, Vol. 31(5), pp. 1026–1033.

Alfredsson, P.H. and Johansson, A.V. 1984. “Time scales in turbulent channel flow”. *Physics of Fluids*, Vol. 27(8), pp. 1974–1981.

Bairstow, L., Cave, B.M., and Lang, E.D. 1923. “The resistance of a cylinder moving in a viscous fluid”. *Royal Society of London Philosophical Transactions Series A*, Vol. 223, pp. 383–432.

Fernholz, H.H. and Finley, P.J. 1996. “The incompressible zero-pressure-gradient turbulent boundary layer: an assessment of the data”. *Progress in Aerospace Sciences*, Vol. 32(4), pp. 245–311.

Große, S., Schröder, W., and Brücker, C. 2006. “Nano-newton drag sensor based on flexible micro-pillars”. *Measurement Science and Technology*, Vol. 17, pp. 2689–2697.

Jeon, S., Choi, H., Yoo, J. Y., and Moin, P. 1999. “Spacetime characteristics of the wall shear-stress fluctuations in a low-reynolds-number channel flow”. *Physics of Fluids*, Vol. 11(10), pp. 3084–3094.

Khoo, B.C., Chew, Y.T., and Li, G.L. 1997. “Effects of imperfect spatial resolution on turbulence measurements in the very near-wall viscous sublayer region”. *Experiments in Fluids*, Vol. 22, pp. 327–335.

Kreplin, H.-P. and Eckelmann, H. 1979. “Behavior of the three fluctuation velocity components in the wall region of a turbulent. channel flow”. *Physics of Fluids*, Vol. 22(7), pp. 1233–1239.

Löfdahl, L. and Gad-el-Hak, M. 1999. “MEMS-based pressure and shear stress sensors for turbulent flows”. *Measurement Science and Technology*, Vol. 10, pp. 665–686.

Madavan, N.K., Deutsch, S., and Merkle, C.L. 1985. “Measurements of local skin friction in a microbubble-modified turbulent boundary layer”. *Journal of Fluid Mechanics*, Vol. 156, pp. 237–256.

Moser, R.D., Kim, J., and Mansour, N.N. 1999. “Direct numerical simulation of turbulent channel flow up to $Re_\tau = 590$”. *Physics of Fluids*, Vol. 11, pp. 943–945.

Naughton, J. and Sheplak, M. 2002. “Modern developments in shear-stress measurement”. *Progress in Aerospace Sciences*, Vol. 38, pp. 515–570.

Press, W.H., Teukolsky, S.A., Vetterling, W.T., and Flannery, B.P. 1992. *Numerical Recipes in C*.

Schlichting, H. 1958. *Grenzschicht-Theorie*. Verlag G.Braun, Karlsruhe, 3. Edition.

Sreenivasan, K.R. and Antonia, R.A. 1977. “Properties of wall shear stress fluctuations in turbulent duct flow”. *Journal of Applied Mechanics*, Vol. 44, pp. 389–395.

Stokes, G.G. 1922. “On the Effect of the Internal Friction of Fluids on the Motion of Pendulums”. *Transactions of the Cambridge Philosophical Society, reprinted in Mathematical and Physical Papers, Cambridge University Press*, Vol. 3, pp. 1–123.

Wietrzak, A. and Lueptow, R.M. 1994. “Wall shear stress and velocity in a turbulent axisymmetric boundary layer”. *Journal of Fluid Mechanics*, Vol. 259, pp. 191–218.